

3 Results

In this “Results” chapter, I first walk through the reference model (M28LinT1) and compare it with a constant M model (M88ConT2). Then, I describe in detail the major characteristics of the models. Finally, I compare the models in terms of 1) two types of the weakening rates; 2) three types of the ranges of M variation and 3) three types of the functional forms of M variation.

3.1 Reference model (M28LinT1 Table 2)

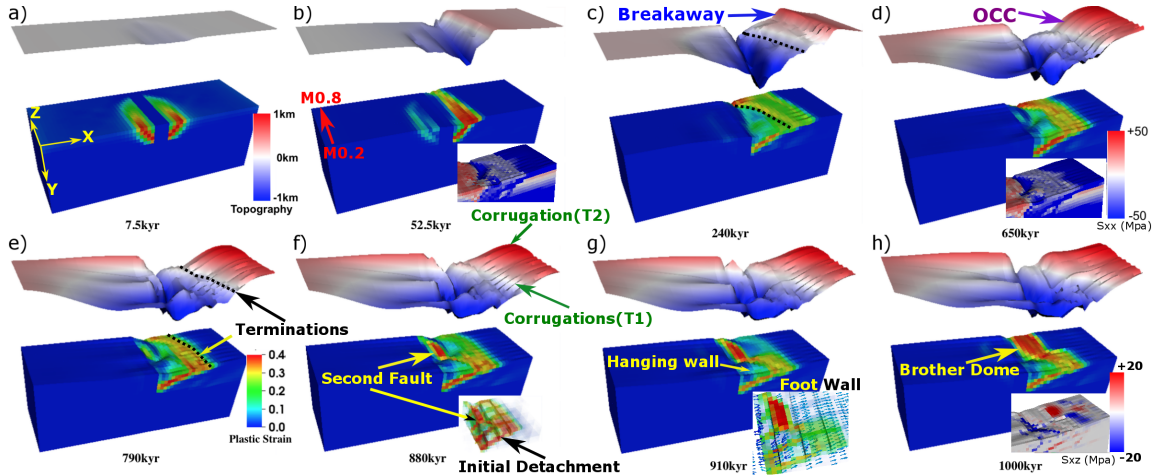


Figure 8: Evolution of plastic strain and surface topography of the reference model M28LinT1: (Table 2). The number with kyr beneath each model result is the model time. The top layer is the five times exaggerated topography of the model with its color scale showing in Figure 8.a. Initial seafloor is marked as a reference of 0 km in height. The color scale of plastic strain is shown in Figure 8.e. The bold dash line marked in Figure 8.c.e) is the termination of the detachment. The two insets in Figure 8.b and Figure 8.d show σ_{xx} (S_{xx} in the figure). Positive value (pink and red) means tension and negative (blue) is compression. The inset in Figure 8.h is for shear stress σ_{xz} (S_{xz} in the figure). The inset in Figure 8.f is a transparent view of plastic strain. The inset in Figure 8.g shows both plastic strain and the velocity vector. Indicated by the velocity vector, the hanging wall of the detachment fault at low M region ($M = 0.2 \sim 0.5$) is moving in an opposite direction (negative x -axis) to its adjacent higher M region ($M > 0.5$).

I consider the model with M varies linearly from 0.2 to 0.8 along the ridge axis with type 1 weakening rate as our reference model (M28LinT1). The major characteristics of

the model are indicated in the Figure 8. They are breakaway (Figure 8.c); dome shape oceanic core complex (OCC)(Figure 8.d); terminations of the detachment where the active faulting interface reaches the seafloor (Figure 8.e); new near ridge axis high angle normal fault termed as “second fault” and type 1 and type 2 corrugations (Figure 8.f) (the type 1 and 2 corrugations has different formation mechanisms as will be described in the following section); and the side-by-side “brother dome” (Figure 8.h).

As shown in Figure 8, the model creates a median valley that widens and deepens with increasing model time (Figure 8.a.b.c). The rate of its widening and deepening at a specific location along the ridge is inverse proportional to the rate of local magma supply (i.e. M value). OCCs with more than one kilometer in relief and tens of kilometers in wavelength are produced in the model. One interesting behavior worth noting is that corrugations with wavelengths of hundred-to-thousand meters and amplitudes of ten-to-hundred meters are also produced in the model.

As shown in Figure 8.a, for the first 7.5 kyr, high angle ($\sim 60^\circ$) normal faults, represented by localized plastic strain, begin to form near the ridge axis. The angles of the faults are consistent with Anderson’s theory of faulting mechanics for a frictional angle of 30° . Stresses due to plate motions accumulate faster at the lower M side than at the higher M side. Due to this M variation, the fault initiates at the lower M side and then propagates to the higher M side. Meanwhile, the along ridge axis coupling forces (i.e. torsion (clockwise); shearing (σ_{xz})) prevent relative displacement between the two neighbors along the ridge axis. These along ridge coupling forces on the other hand assist in fault propagation from the lower M side ($M = 0.2$) to the higher M side ($M = 0.8$) and reduces the time difference in the initiation of faulting along the ridge axis when comparing with separated pseudo-2D models.

At 52.5 kyr (Figure 8.b), the normal fault on the right hand side of the ridge axis continues to evolve while the one on the left becomes inactive. The choice of which fault to develop seems to be made due to a small numerical perturbation between the two faults

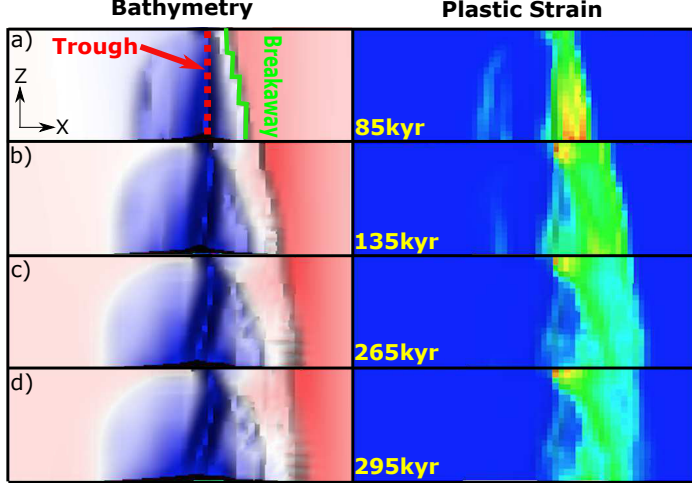


Figure 9: Breakaway (marked by green bold line) and trough (marked by red dash line in (a)) evolution with time in bird's-eye view (M28LinT1 (Table 2)). Left column is topography at different model time; right column is plastic strain. They both share the same color scales as in the Figure 8. The offset in x -axis direction between breakways along the ridge axis maintains ~ 3 km until 295 kyr. It also shows that the lowest topography points along the ridge axis (“trough inside the median valley”) start as a straight line parallel with ridge axis in (a) and then gradually become oblique to the ridge axis (b.c.d). Please see text for detail description.

seen in Figure 8.a although the model setup is symmetrical across the ridge axis. The timing difference of initiation of faulting along the ridge axis creates an offset in the x -axis direction between the breakaways along the ridge that the breakaway at the lower M side extends further than that of the higher M side (Figure 9). The offset is maintained because the extending velocity of the breakaways to move away from the ridge axis is controlled by the far field extension rate, V_x . The plastic strain also shows similar along ridge offset in x -axis direction. However, the along ridge offset in x -direction of the tips of the extending plastic strain reduces at ~ 295 kyr (Figure 9.d) because once the detachment fault at the lower M side bends to its lowest dip angle, the termination of the detachment fault stops extending and the healing effect implemented in the model reduces quickly the plastic strain of the inactive fault interface that has been exhumed to the seafloor while at the higher M side, the termination keeps extending and reduces the initial offset generated by the asynchronous initiation of faulting. In addition, as shown in the inset of (Figure 8.b),

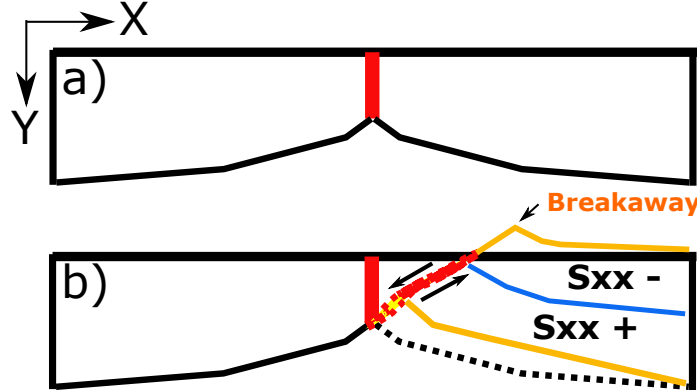


Figure 10: Bending stress illustration. The blue line is the neutral plane where $\sigma_{xx} = 0$. Above the neutral plane is compression ($\sigma_{xx} < 0$) and beneath it is tension ($\sigma_{xx} > 0$). Due to sea water pressure and lithostatic pressure, compression is generally one degree magnitude larger than tension.

as the fault slips, crust at the footwall bends in a clockwise rotation as illustrated by Figure 10. The neutral plane ($\sigma_{xx} = 0$) is shown as the boundary between blue (compression) and pink (tension) (inset of Figure 8.b).

At 240 kyr (Figure 8.c), the median valley further deepens and widens. The detachment keeps slipping and as it bends, the termination at the lower M side ($M < 0.3$) extends ~ 15 km away from the ridge axis with the dip angle decreases from initially $\sim 60^\circ$ to $\sim 30^\circ$ at the root of the fault and to $\sim 0^\circ$ at the exposed fault interface. However, for the detachment at the higher M side (especially for $M > 0.7$), the dip angle remains high and the termination of the detachment is closer to the ridge axis. The maximum relief between highest point at the breakaway and lowest point inside the median valley becomes larger than 1 km. In addition, ~ 1 km wavelength type 1 corrugations begin to show up between the breakaway and termination at the lower M side ($M < 0.3$). The trough inside the median valley evolves from a straight line parallel to the ridge axis (Figure 9.a) to a line oblique to the ridge axis and the obliquity increases with model time (Figure 9.b,c,d).

At 650 kyr (Figure 8.d), the median valley becomes wider and deeper. The detachment fault reaches its lowest dip angle with its termination begin to maintain stable (not extending further). The breakaways along the ridge axis already moved out of the model

domain. The fault slip is already larger than the thickness of the crust and the upper mantle materials are exhumed to the surface. The previous fault interface bends over to a negative dip angle (dip away from the ridge axis) and produces a dome shape OCC with corrugations on its surface parallel to the spreading velocity. Compared to the inset in Figure 8.b, the total length of the bending crust decreases. A hint of a near-axis second fault begins to initiate at the higher M side ($0.5 < M < 0.65$).

At 790 kyr (Figure 8.e), the hint of the second fault evolves and propagates toward higher M side. However, the initial detachment fault is still active and most of the extension at the higher M side ($M > 0.5$) is still taken up by it. The termination of the detachment fault marked in the figure shows along ridge variation in distance to the ridge axis. Basically the lower M side ($M < 0.5$) extends further than the higher M side ($M > 0.5$) because the detachment fault at the higher M side remains in higher dip angle due to less fault slip which results from more magma supply. This along ridge variation produces three type 2 corrugations (it will be further explained in the next section). One has a wavelength of ~ 6 km with an amplitude of several hundred meters. The other two are on the surface of the first corrugation with wavelengths of less than 1 km and amplitudes of several tens of meters.

At 880 kyr (Figure 8.f), at the higher M side ($M > 0.5$), the hint of the second fault evolves to a high angle near-axis normal fault and replaces the initial detachment fault as indicated in the inset of transparent view of plastic strain. All the extension is now taken up by the second fault.

At 910 kyr (Figure 8.g), the second fault results in a strong contrast in velocities between higher M side and lower M side that at the higher M side, previous hanging wall becomes footwall and moves with the spreading plate to the positive x -axis direction, however, at the lower M side, due to deficit in magma supply, the hanging wall (indicated in Figure 8.g) is coupled with the conjugate plate and moves toward the negative x -axis direction as shown in the inset of the velocity field of the model. This opposite directions

of velocities result in a dextral shear stress σ_{xz} region aligns with the termination of the detachment fault at the lower M side ($M < 0.5$). It is $\sim 45^\circ$ oblique to the ridge axis (inset of Figure 8.h) and it produces a new trough inside the median valley that aligns with it. Combined with the previous trough, an “X” shape topography low is created in the model.

3.1.1 Constant M along the ridge axis (M88ConT2 Table 2)

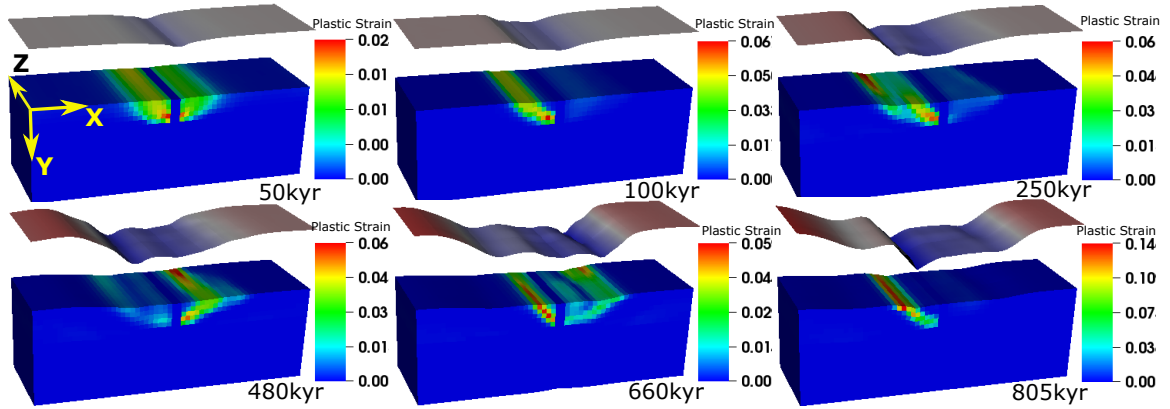


Figure 11: Evolution of plastic strain and surface topography of the model: M88ConT2 (Table 2).

As a comparison to the varying M models, a constant M model is run.

As shown in Figure 11, model M88ConT2 produces a ~ 20 km wide and $1\sim 2$ km deep median valley. It is similar to the generally observation of the Mid-Atlantic Ridges. The width and depth of the median valley is almost constant along the ridge axis as contrast to the varying M models. The variations along the ridge axis in breakaway, termination as well as the corrugation mentioned in the reference model (M28LinT1) are not produced.

Because the magma supply is constant along the ridge with $M = 0.8$, there is no along ridge axis variation in the rate of tensional stress accumulation. Thus, the normal faults along the ridge initiate at the same time and the slipping rate of the fault is also constant along the ridge axis. The synchronized fault initiation results in no offset between breakaways and the constant slipping rate produces no along ridge axis variation in the position

of the termination. Thus, neither type 1, type 2 corrugations nor along ridge axis variation in width and depth of the median valley are generated.

Normal faults alternate on each side of the ridge axis with a period of ~ 300 kyr due to the mechanism mentioned in the “Introduction” section for the 2D models of $M > 0.5$. This fault alternation produces the symmetrical high frequency abyssal hills. For 3D models, why and how fault alternates on each side of the ridge axis is slightly different than the previous 2D studies. It will be further described in the following section.

3.2 Main characteristics of the models

3.2.1 Location of termination

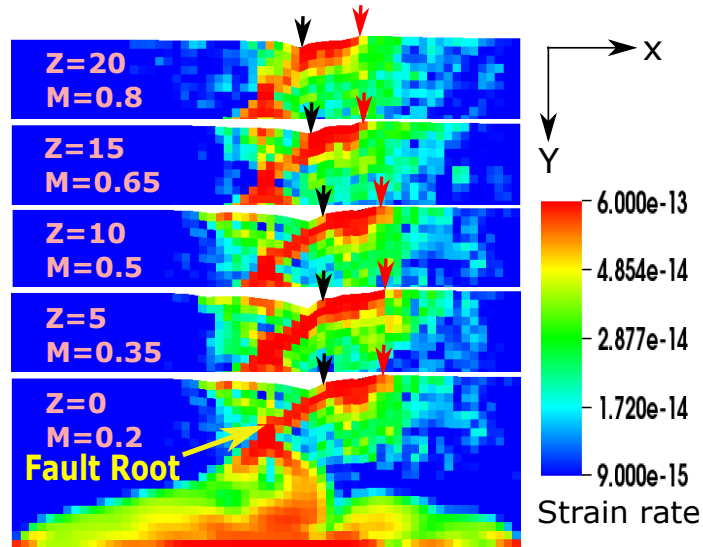


Figure 12: Five slices of strain rate along the ridge axis for the model M28LinT1 (Table 2) at 107.5 kyr. The 5 terminations and 5 breakaways along the ridge axis are marked by the 5 black and 5 red arrows respectively.

The location of the termination (bold dash line in Figure 8.c.e)) of the detachment fault where footwall begins to be exhumed to the seafloor varies along the ridge axis. As shown in Figure 12, the highest strain rate regions (red) can be interpreted as the active detachment fault interfaces. When $M \leq 0.5$, although the rate of fault slip should be higher for lower M , the rate of bending of the hanging wall or the rate of decreasing in

dip angle of the detachment fault has a maximum value that corresponds to the far field extension rate V_x . Because for $M < 0.5$ (Figure 12, (M = 0.2, 0.35, 0.5)), the detachment fault roots at the same place (marked in the slice of M = 0.2) at the intersection between the center dike and the brittle-ductile transition (BDT), the amount of bending in the footwall of the detachment fault is determined by how far the termination extends away from ridge axis. In other words, because in order to spend least frictional energy during faulting, the detachment fault interface between the two ends (termination and root) tends to be a straight line. Thus, the dip angle of the fault is inverse proportional to the distance between the termination and the root of the normal fault when $M < 0.5$. So the farther the distance between the termination and the root of the fault, the lower its dip angle. Since the breakaways at the lower M side ($M < 0.5$) moves with the extending plate under the same velocity V_x , and the initiation time difference of the normal faults at the lower M side is similar (Figure 8.a), the distances between the breakaways and the roots of the faults are the same. Meanwhile, the distance between breakaways and terminations as indicated by the red and black arrows in the Figure 12 is the same along the ridge axis. Thus the dip angles of the faults at the same time along the ridge-axis are the same. However, when $M > 0.5$ (Figure 12, (M = 0.65, 0.8)), the amount of fault slip decreases as M increases. The crust at the footwall experiences less bending and the detachment fault remains in a higher angle as well as that the terminations are closer to the ridge axis. Because the root of the fault is slowly pushed away from ridge axis while the breakaways of the faults are closer to ridge axis due to a later initiation of the fault. In addition, the crust thickness that the fault cuts through is slowly increasing as the fault being pushed away from ridge center due to excessive diking. These three factors together contribute to a higher dip angle. In a unit time, the volume of the exhumation is also smaller for the higher M side. One thing needs to be noted is that the trough at the higher M side correspond to the terminations but detached from the terminations at the low M side ($M < 0.5$) as shown in Figure 12.

3.2.2 Geometry of trough

The lowest topography points inside the median valley evolves from a straight line parallel to the ridge-axis (Figure 9.a) to a line oblique to the ridge-axis (Figure 9.b,c,d). Initially, the lowest topography points are at the terminations of the detachment fault. Due to the coupling along the ridge-axis, fault propagates from front to back in a straight line parallel to the ridge-axis. However, as the dip angle of the detachment at the low M side begin to decrease due to bending of the crust at the footwall, along with excessive tensional stress results from low magma supply, the lowest topography point at the lower M side is pulled to the conjugate plate. While the lowest topography points at the high M side ($M > 0.5$) are pushed away from the dike. Note that the oblique lowest topography points form not a straight line, but a curve that the lowest point remains near the ridge-axis at the high M side. This is due to the bending rate of the detachment at high M side is very low and thus the termination can remains near the ridge-axis.

XT:One question needs to be answered: at 410 timesteps (205kyr), the breakaway at the front already extends 15km. If assumming a constant extending rate, it means a velocity of around 75km/Myr, much faster than half spreading rate 25km/Myr. If it is true, I need to change previous discussion on how fast breakaway being pulled away from ridge-axis.

3.2.3 Second fault

3.2.4 Fault alternation

3.2.5 Cut-back

3.2.6 Corrugations

Corrugations due to anastomosing

Corrugations due to asynchronous normal faulting

3.3 Effects of the functional forms of M variation

As shown in the ~~EC:~~tables [which table? Specify.], ~~EC:~~the models with ~~EC:~~M28 [Before starting to use this notation, define and explain it first!] with type 1 weakening is ~~EC:~~the only M range that has three functional forms data points available [This sentence gives an impression that you didn't want to use these three but had no choice but to. This is not the case, I believe. Probably you'd want to point out that one of these three is the reference model that has been fully described earlier. So, we are in a better position to compare it with similar models with different functional forms. In fact, I think this introductory sentence can be thrown out.]

~~EC:~~There are two phenomena that show distinct differences with respect to different functional forms. By comparing M28LinT1 with M28SinT1 and M28sqrtT1, I identified two main characteristics in the different behaviors of these models due to different functional forms of M variation. One is the geometry and timing of the secondary fault. The other is the “Cut back” behavior. ~~EC:~~mostly observed in the square root model. [No need to spill the beans.]

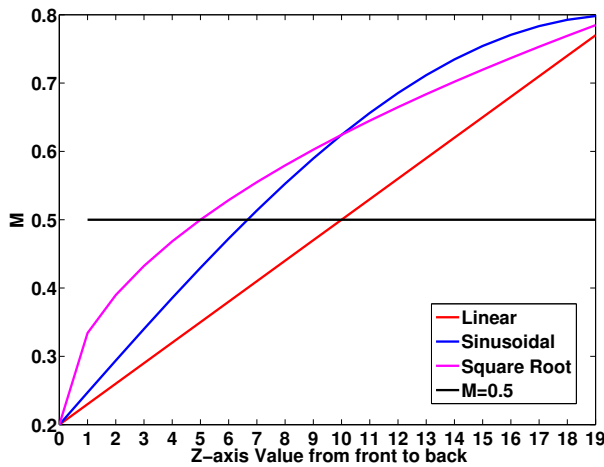


Figure 13: Three functional forms of M variation comparison. They begin to exceed the $M = 0.5$ black line at $Z=10, 7, 5$ for linear, sinusoidal and square root respectively.

Second Fault For the linear functional form, the second fault ^{XT}: [add a definition of secondary fault in the begining, here add a link of figure about primary and sec fault, enlarge the second fault and add label in the figure and use it here] at the high M side has started accommodating most of the extension at around 900 kyr and the initial detachment becomes inactive ^{XT}: [(Figure 14)]refer to Figure 8.f is better. It nucleates from the ridge center where $M = 0.5$ and then propagates to the $M = 0.8$ end.

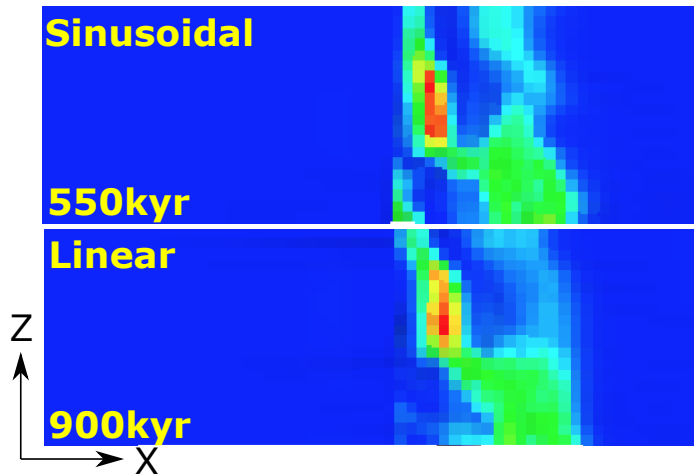


Figure 14: M28LinT1 versus M28SinT1 (Table 2). Secondary fault length comparison between linear and sinusoidal. Around 13 elements in length for sinusoidal compared to 11 elements for linear.

For the sinusoidal form, the second fault begins to form at a much earlier time around 550 kyr (Figure 14). The sinusoidal form consistently has higher M values than the linear form (Fig. 10), implying a greater amount of magma supply. The first forming fault moves away from the ridge axis faster and locks earlier in the case of the sinusoidal form. As a result, the second fault appears earlier than in the case of the linear M variation. In addition, the sinusoidal form produces the second fault with a greater along-strike dimension than the linear form because this length is proportional to the length of the $M \geq 0.5$ portion of the ridge (Figure 13). For square root, there is no secondary fault forming because the “cut back” behavior releases the tensional stress in the hanging wall.

Cut-back ^{XT}: [Define a cut-back and think about a different name.] The cut-back char-

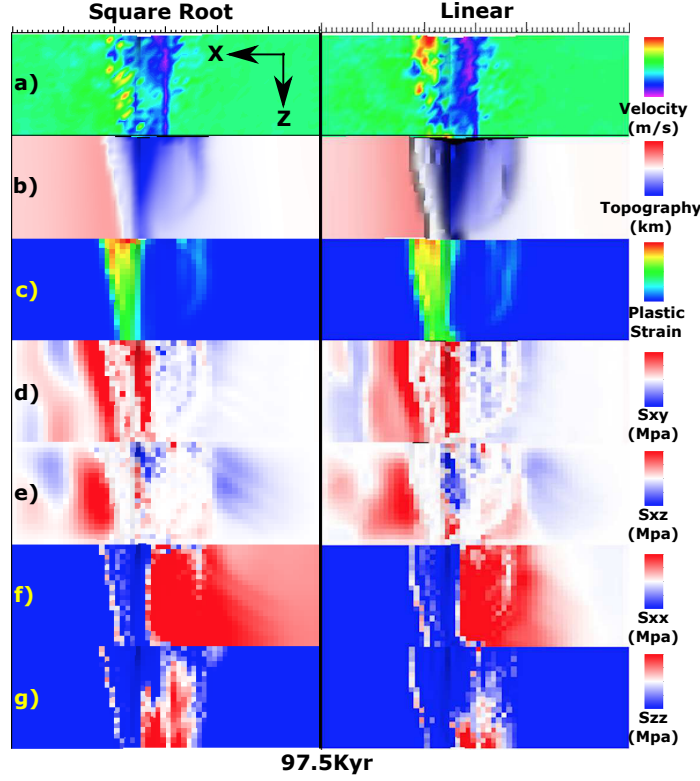


Figure 15: M28LinT1 versus M28SqrtT1 (Table 2) at 97 kyr. View from top of the model.

acterizes but are not limited to the models with the square root form of M variation.^{XT:} [exclusively about the square root models?] As shown in Figure 15, Figure 16 and Figure 27^{XT:} [Bring up Fig. 26 here and include only the cut-back panel.], between 97.5 kyr and 100 kyr, there are cut-backs in the square root model M28SqrtT1 at the low M side where hanging walls with surface area of $\sim 60 \text{ km}^2$ and $\sim 120 \text{ km}^2$ (the red block) suddenly rebound backwards towards the ridge axis as seen in 100 kyr and 160 kyr (Figure 16.a and Figure 27.d,e,f), along with sudden topography drop (Figure 27.d,e 2nd row), σ_{xy} and σ_{xz} released, termination falls back (Figure 27.f 3rd row).

3.4 Effects of the weakening rate

According to our available twelve 3D models, we have three pairs of models that both have type 1 and type 2^{XT:} [might want to add a ref to the section defining these.] weakening while the range of M and functional form are maintained to be the same. They are

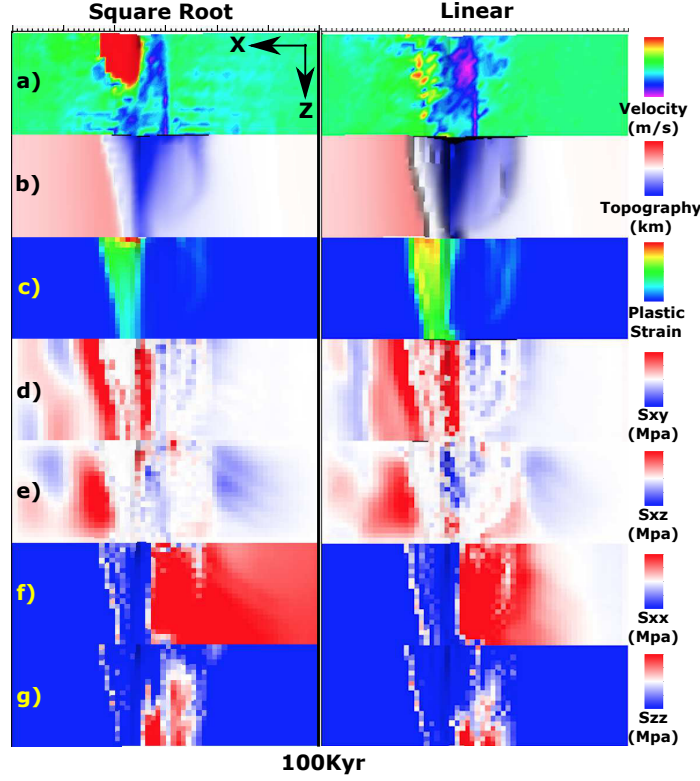


Figure 16: M28LinT1 versus M28SqrtT1 (Table 2) at 100 kyr. View from top of the model.

M57SinT1/T2, M58SinT1/T2 and M58SqrtT1/T2.

M57SinT1 versus M57SinT2 Initially, both models develop normal faults on both sides of the ridge axis^{XT: [no hyphen in “ridge axis”.]} at the low M side. In the model with the faster weakening rate (M57SinT1), faults propagate toward the high M side and cut through the whole crust by 25 kyr but this process completes later at 50 kyr in the model with the slower weakening rate (M57SinT2). At around 310 kyr, the second fault appears at the high M side^{XT: [instead of z=5, use a M value.]} of M57SinT2 while where $M \leq 5$ [some M value], the initial fault remains active (Figure 17.a) and b)). However, when the weakening is fast (M57SinT1), cut-back happens at around 260 kyr and help to maintain a high angle fault with closer to ridge axis termination. The initial fault remains, no secondary fault forming (Figure 17.a) and b)). In addition, the width of median valley at low M side is wider for M57SinT2 than M57SinT1 (Figure 17.a) and b) versus c) and

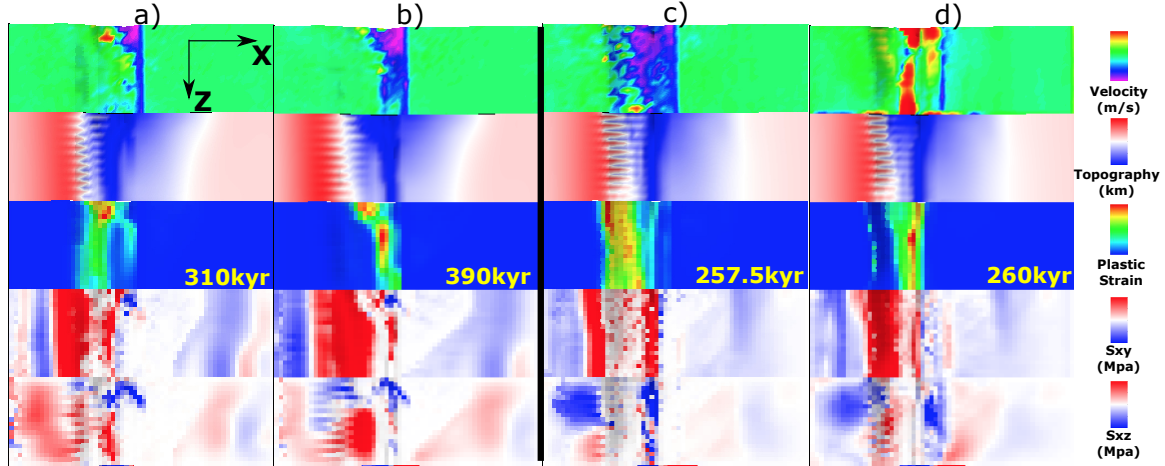


Figure 17: M57SinT2 versus M57SinT1 (Table 2). a) and b) are for M57SinT2, c) and d) are for M57SinT1.

d)) due to slower weakening (type 2) allows a more distributed tensional stress σ_{xx} rather than fast weakening that once a fault is established, larger amount of tensional stress σ_{xx} will be released at the fault.

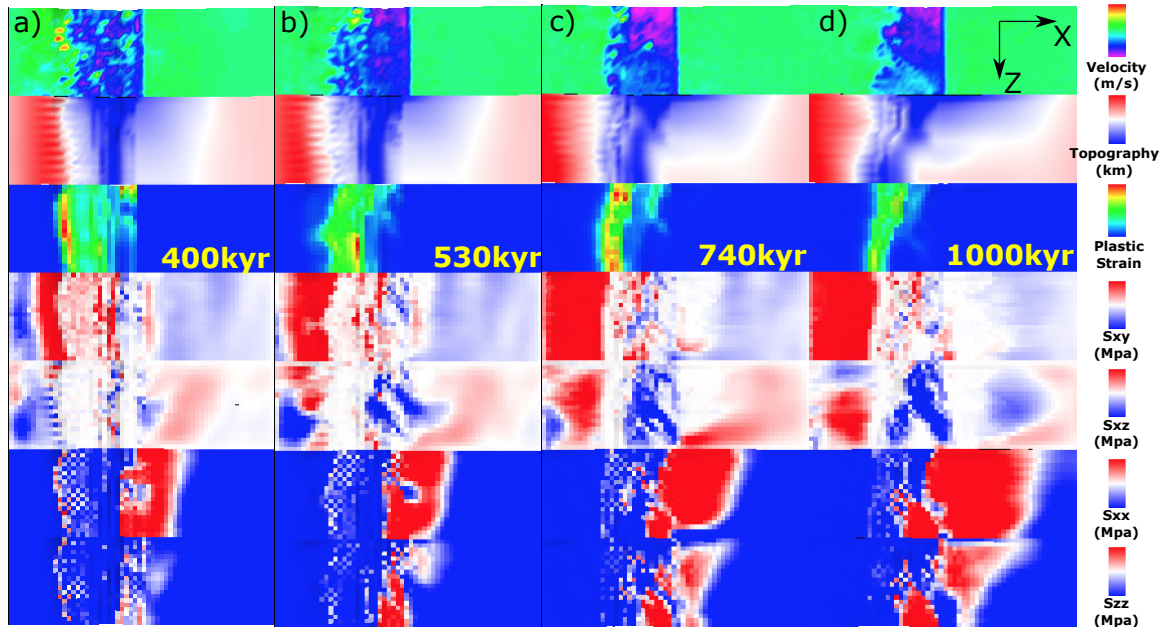


Figure 18: M57SinT1 (Table 2) faulting and stress evolution with respect to time.

M57SinT1 For M57SinT1, as shown in Figure 18, at 400 kyr (Figure 18.a), there is an antithetic fault forming at the low M side accommodating part of the extension, which re-

sults in a curved termination at the far frontier. As it evolve (530 kyr (Figure 18.b)), the termination at the low M side further recedes backward while the termination at the center ($Z = 11 \sim 13$) extends further. This curved termination leads to a curved topography (white curve in the second row). As the fault evolves and bends further away from the axis, at the time of 740 kyr, another antithetic fault forming again at the low M side (Figure 18.c). It doesn't take the place of initial fault and disappear soon, however, it again releases tensional stress and results in that the termination at far front recedes backward. At 1000 kyr (Figure 18.d), an Atlantiss Massif shape OCC is produced (low M side (lower magma supply) has a wider dome and high M side (higher magma supply) has a narrower dome) due to the along ridge axis termination evolution. Corrugations with wavelength varying from hundreds to kilometers are also created.

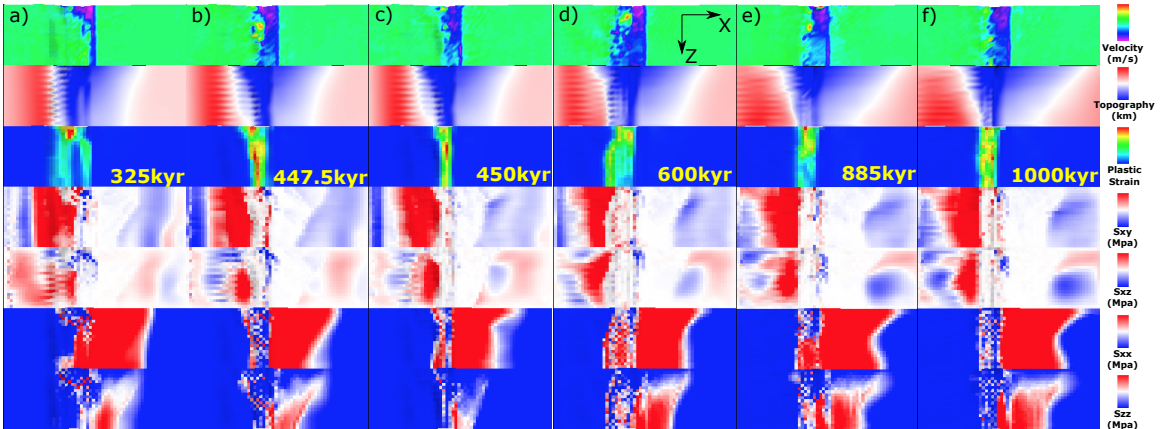


Figure 19: M57SinT2 (Table 2) faulting and stress evolution with respect to time.

M57SinT2 For M57SinT2, as shown in Figure 19, instead of maintaining one fault all the time for M57SinT1, it creates secondary fault at high M side with different mechanism several times. A secondary fault is created at 325 kyr (Figure 19.a), when a new near axis normal fault take the place of the initial one at high M side. Between 447.5 kyr (Figure 19.b) and 450 kyr (Figure 19.c), termination falls back, and as it evolve, termination at the high M side extends further at 600 kyr (Figure 19.d). At 885 kyr (Figure 19.e), a secondary fault propagates from low Z to high Z and terminates the further extended fault at

high Z and maintain a near ridge axis termination.

3.4.1 M58SinT1 versus M58SinT2

A major difference between M58SinT1 and M58SinT2 is that M58SinT1 keep faulting at one side of the ridge axis while M58SinT2's fault alternates.

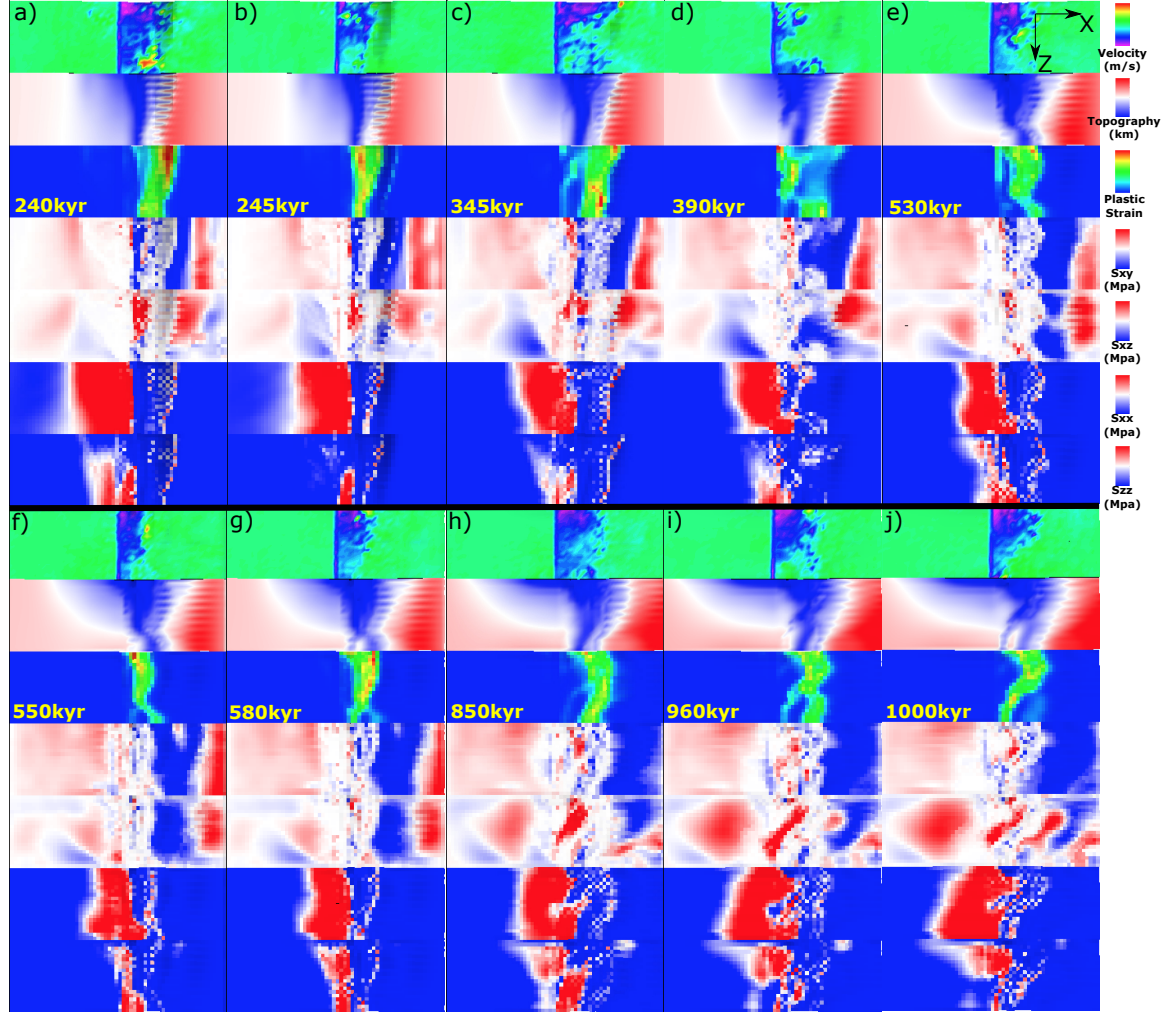


Figure 20: M58SinT1 (Table 2) faulting and stress evolution with respect to time.

M58SinT1 As shown in Figure 20, in 1Myr, the fault keeps on the right hand side of the ridge axis. It evolves dynamically. Between 240 kyr (Figure 20.a) and 245 kyr (Figure 20.b), there is a cut back. At 345 kyr (Figure 20.c), at low Z side, there are two offset antithetic faults ($Z=1 \sim 2$ and $Z=5 \sim 9$) in the hanging wall begin to evolve and

soon connect to each other forming anastomosing fault zone. At 390 kyr (Figure 20.d), the new near axis anastomosing fault zone replace the old further away from ridge axis detachment. There is dextral σ_{xz} forming on the right hand side of the new anastomosing fault zone ((Figure 20.d), row 5) due to the offset between the new near axis fault at low Z side and extended further fault at high Z side and leads to the development of a $\sim 45^\circ$ shear zone connection between the new near axis fault zone at low Z side and the further away from axis original detachment at high Z side. It also creates a curved termination which will lead to a curved topography (boundary between blue and white) seen at 530 kyr (Figure 20.e). Note that this curved termination can be a mechanism for producing large wavelength (several kilometers) undulating corrugations. Between 530 kyr (Figure 20.e) and 550 kyr (Figure 20.f), there is another cut back happens. Terminations fall backwards to near ridge axis position. At 580 kyr (Figure 20.g), at the high Z side, a new near ridge-axis high angle normal fault begin to initiate under the assistance of rotational force from low Z side due to along ridge axis coupling. This produces a large rider block with several kilometers in its length scale. Previous “S” curved termination now evolves to a half circle curve and it soon affects the curve of topography as seen at 850 kyr (Figure 20.h). Due to along ridge axis variation in diking, a large sinistral shear zone (red region $\sim 40^\circ$ oblique to ridge axis seen in 5th row of 960 kyr (Figure 20.i)) keep developing and cut the circle curved fault zone at 850 kyr (Figure 20.h) into a new fault zone with higher curvature as seen in 1000 kyr (Figure 20.j).

M58SinT2 As shown in Figure 21, the fault initiates on the left hand side of the ridge axis (Figure 21.a). Low Z side extends further than high Z side. It takes around 100 kyr to form into a localized fault plane due to slower rate of weakening. At 215 kyr (Figure 21.b), another fault on the conjugate plate begin to evolve and replaces the initial one. As seen from (Figure 21.b), corrugations are created at low Z side. At 330 kyr, a third fault forming at the left hand side of the ridge axis. Between 490 kyr (Figure 21.d) and

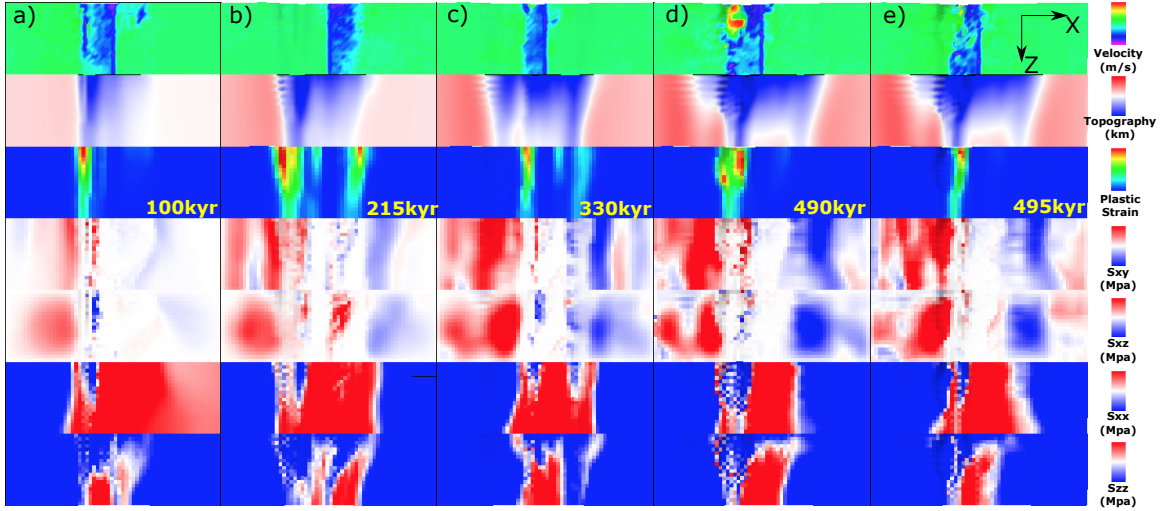


Figure 21: M58SinT2 (Table 2) faulting and stress evolution with respect to time.

495 kyr (Figure 21.e), there is a cut back.

3.4.2 M58SqrtT1 versus M58SqrtT2

The major difference between M58SqrtT1 and M58SqrtT2 is also whether the normal fault alternates or not.

M58SqrtT1 As shown in Figure 22, initially, there is a 5 element offset between breakaways along the ridge axis due to along ridge axis variation in diking (Figure 22.a). At 370 kyr (Figure 22.b), there is a vertical tensile failure at $Z= 1 \sim 2$. Two parallel dextral (blue) shear regions are seen (5th row). The low Z shear zone assists in the shear failure observed at 400 kyr (Figure 22.c), and it develops into near ridge axis normal fault ($Z=4 \sim 12$) and propagates to high Z side which eventually cuts through and reaches $Z= 20$ and replaces the initial extended fault at high Z side at 460 kyr (Figure 22.d). The vertical tensile failure zone at $Z= 1 \sim 3$ (Figure 22.d 3rd row) begin to evolve and assists in the initiation of a new near ridge axis high angle normal fault which connect with the fault at the high Z side (Figure 22.e) at 590 kyr. At 660 kyr (Figure 22.f 3rd row), there is a hint of high angle normal faulting at $Z= 1 \sim 3$ of conjugate plate. But it doesn't develop. At 730 kyr (Figure 22.g 5th row), a dextral (blue) shear zone at the low Z side help

to create the faulting pattern seen at 780 kyr (Figure 22.h 3rd row), a concave termination with a wavelength of 10 kilometers and it has the potential to create a large wavelength corrugation. Meanwhile, at the low Z side, near the ridge axis, there is an antithetic fault forming at the hanging wall of the detachment and it later propagates to high Z side (Figure 22.i). From 820 kyr to 880 kyr, the antithetic fault evolves to near ridge axis normal fault and connects with the detachment at the high Z side (Figure 22.j). In addition, a tensile failure shows its hint at the low Z side ($Z = 1 \sim 5$) of the conjugate plate.

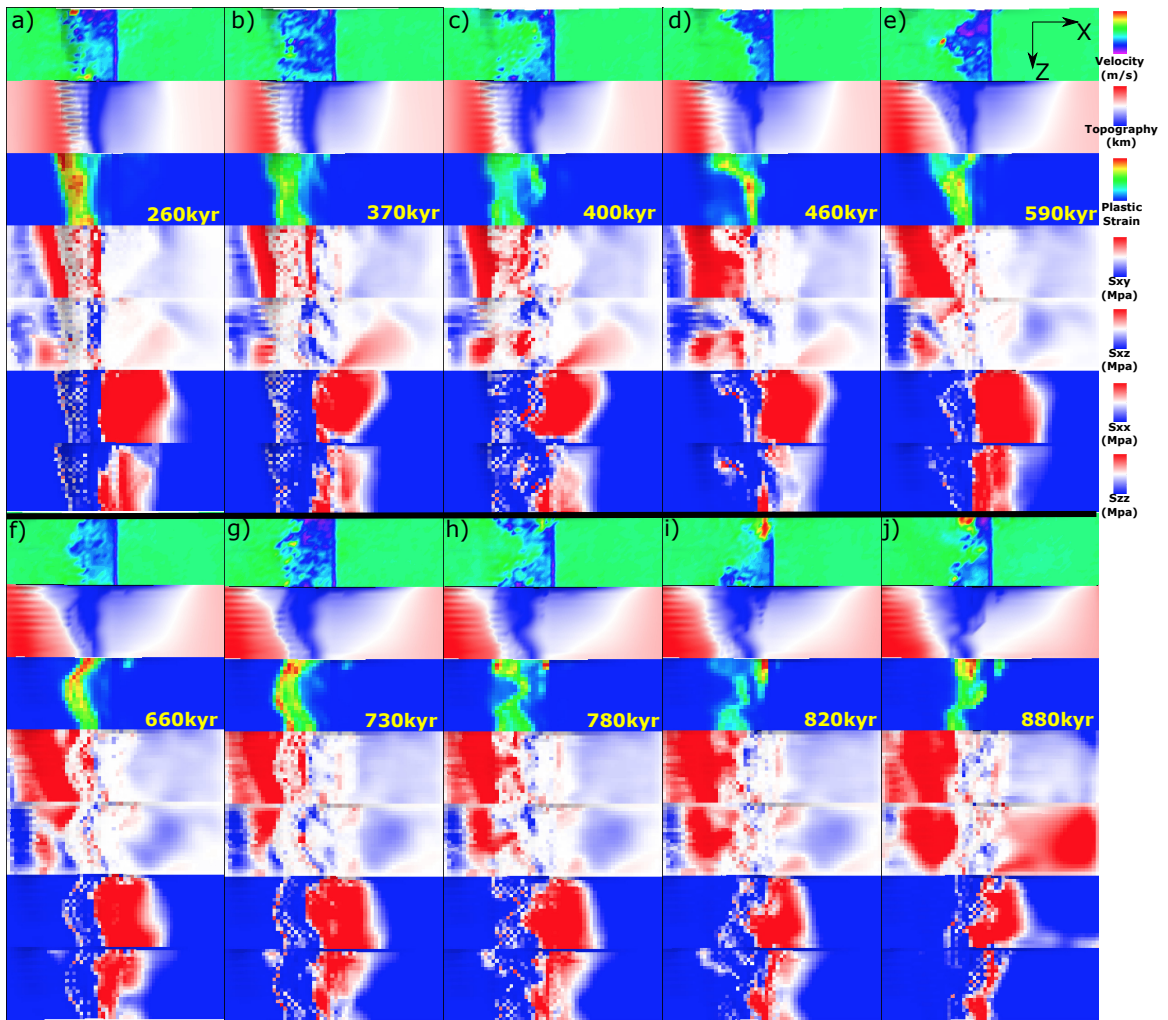


Figure 22: M58SqrtT1 (Table 2) faulting and stress evolution with respect to time.

M58SqrtT2 As shown in Figure 23, at 195 kyr (Figure 23.a), due to transtensional stress at low Z side ($Z = 1 \sim 6$), several corrugations begin to evolve. At conjugate

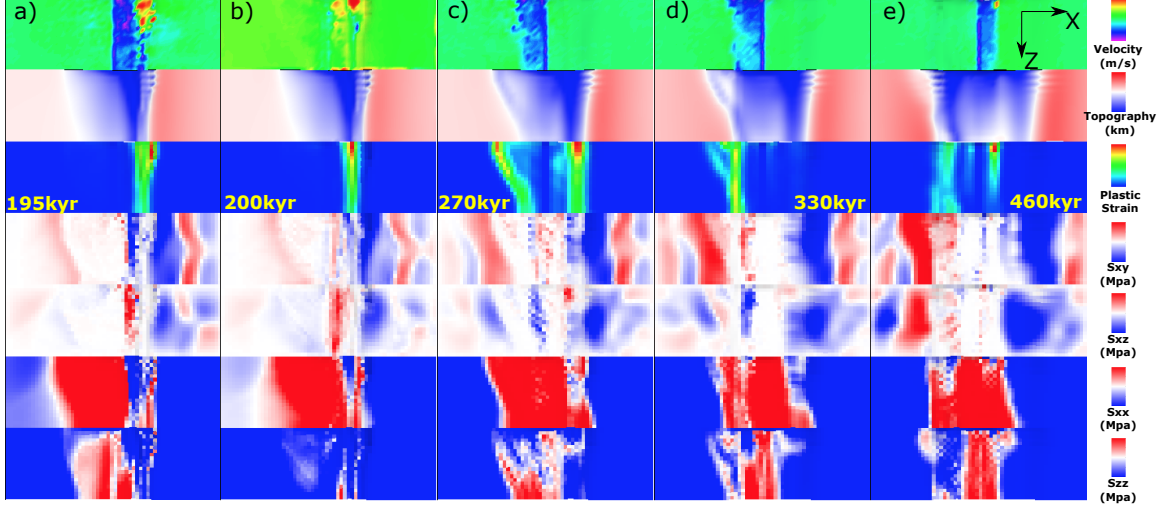


Figure 23: M58SqrtT2 (Table 2) faulting and stress evolution with respect to time.

plate, dipping toward axis shear zone σ_{xy} (red at 4th row) show its curve and keeps accumulating. σ_{xx} is also accumulating on the conjugate plate. Between 195 kyr (Figure 23.a) and 200 kyr (Figure 23.b), there is a cut back. At 270 kyr (Figure 23.c), immediately above and following the curved shape shear σ_{xy} zone on the left hand side of the ridge axis, a new fault begin to evolve and replace the initial fault on the right. At 330 kyr (Figure 23.d), at the low Z side, a new near axis high angle normal fault take the place of initial further away from ridge axis fault partly due to rotational force from along ridge coupling. At 460 kyr (Figure 23.e), another normal fault begin to evolve on the right hand side of the ridge axis.

3.5 Effects of the range of M variation

So far, we have three ranges for M variations along the ridge axis (M28, M57 and M58) with same segment length of 20km. Among the 12 available models, two M58 models and the constant $M= 0.8$ model with type 2 weakening produce fault alternation while others do not. Generally, M57 and M58 models create a median valley much narrower and shallower than that of M28 models. $\frac{dM}{dz}$ is larger for M28 than M58 and M57.

3.5.1 M28SinT1 versus M57SinT1 versus M58SinT1

M57SinT1 versus M58SinT1 For description of M57SinT1 evolution with respect to time, please refer to Section 3 and Figure 18. For description of M58SinT1 evolution with respect to time, please refer to Section 3.4.1 and Figure 20. Comparing M57SinT1 and M58SinT1, the major difference is that the faulting pattern evolution for M58SinT1 is much more dynamic with a higher frequency of secondary faults, cut back and offsetted fault segments connection. For M58SinT1, the new secondary near ridge axis normal or antithetic faults usually replace the existed one. However, for M57SinT1, diking is not strong enough to create big enough stress perturbation along the ridge axis for secondary or antithetic faults to take the place of the original one. At the low Z side, near ridge axis antithetic fault only helps to accommodate tensional stress which help maintain a high angle normal fault with near to ridge axis termination while the termination at the high Z side gradually move off axis. This creates a OCC with larger dome at lower magma supply side than that of higher magma supply side which is opposite to the shape of OCC created by M58SinT1.

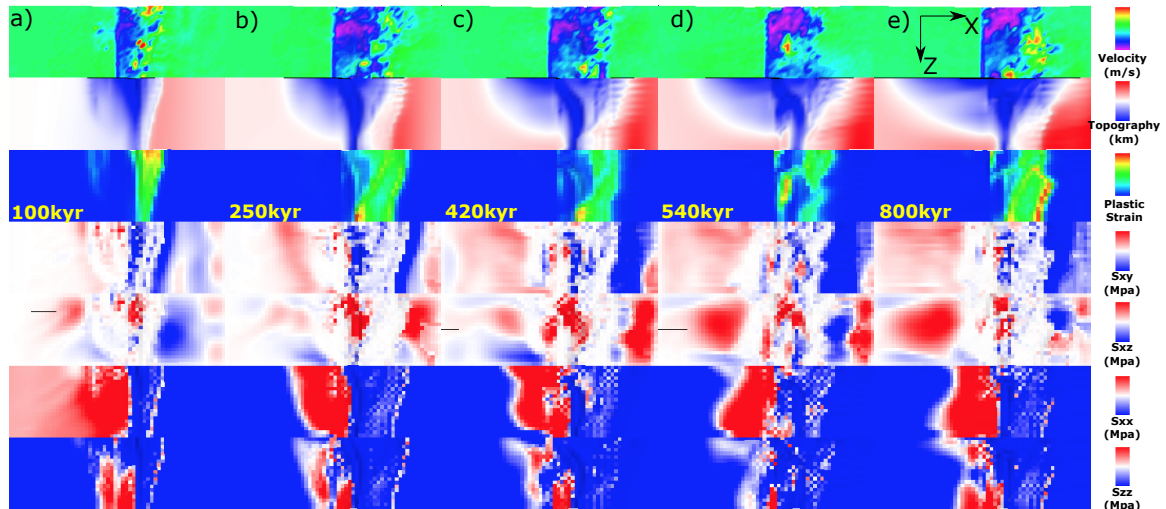


Figure 24: M28SinT1 (Table 2) faulting and stress evolution with respect to time.

M28SinT1 As shown in Figure 24, faulting evolution is much less dynamic than that of M58SinT1. Faulting keeps on the right hand side of the ridge axis. Only one secondary fault is formed at around 540 kyr (Figure 24.d). Initially, at 100 kyr (Figure 24.a), at the low Z side, the normal shear zone at conjugate plate takes up part of the extension and leave a dent in the topography. But it doesn't last long. The initial breakaway of the detachment extends further away from ridge axis with four elements in along ridge axis offset at 250 kyr (Figure 24.b). At 420 kyr, at the high Z side, a hint of new near ridge axis high angle normal fault begin to show up. It develop into a secondary fault at 540 kyr (Figure 24.d) and propagates toward high Z side. This results in a sinistral shear zone (red region in 5th row). At the low Z side ($Z = 1 \sim 3$), a tensile failure can be seen and it take up part of the extension at the low Z side which results in the recede of termination at the low Z side as seen at 800 kyr (Figure 24.e) while the termination at higher Z side extends further away from the ridge axis.

3.5.2 M57SinT2 versus M58SinT2

For description of M57SinT2 evolution with respect to time, please refer to Section 3 and Figure 19. For description of M58SinT1 evolution with respect to time, please refer to Section 3.4.1 and Figure 21. A major difference is that M57SinT2 does not create alternating normal faults on each side of the ridge axis while M58SinT2 does. *XT: Why this seemingly small change could lead to such a to the first order difference in model behaviors?*

3.5.3 M28LinT1 versus M57LinT1

For description of M28LinT1 evolution with respect to time, please refer to Section 3.1.

M57LinT1 As shown in Figure 25, between 160 kyr (Figure 25.a) and 162.5 kyr (Figure 25.b), there is a cut back. The corrugation is very severe and have a discrete distri-

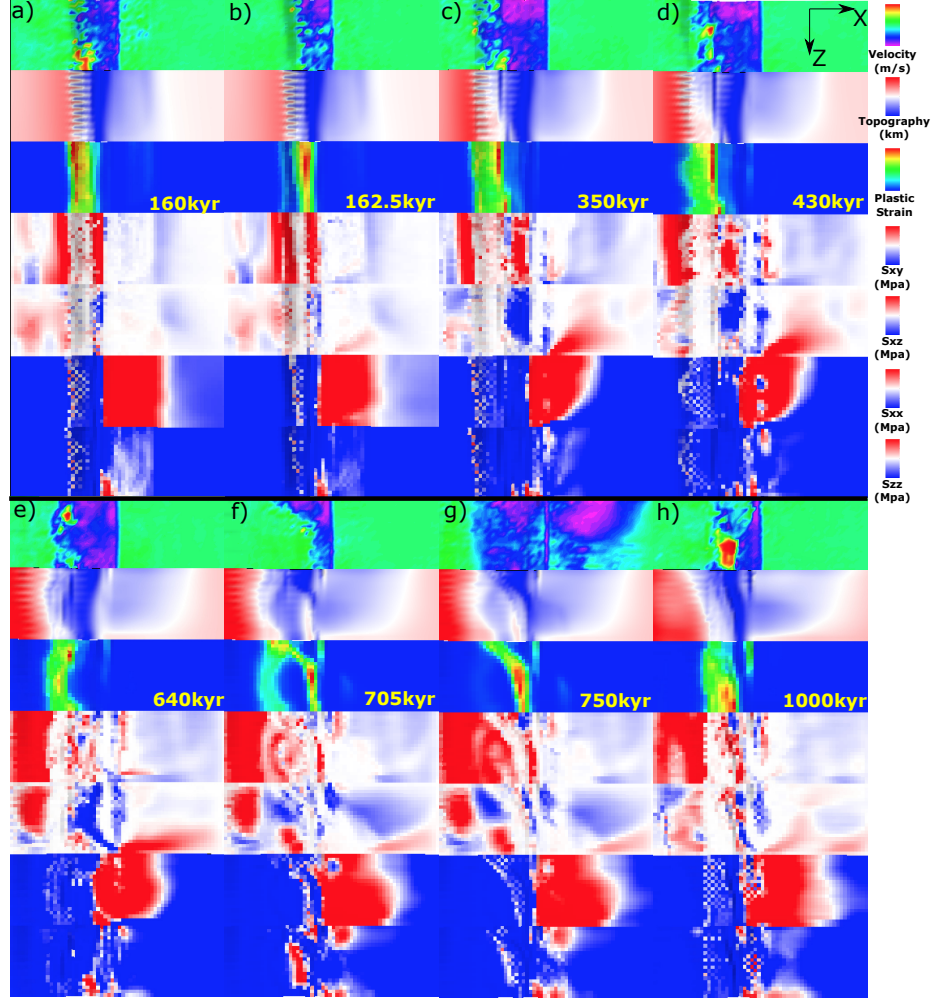


Figure 25: M57LinT1 (Table 2) faulting and stress evolution with respect to time.

bution with one element width as its wavelength. The frontier of breakaway also shows discrete distribution of σ_{xx} and σ_{zz} alternating between tension and compression which might be the reason for the undulating topography. At 350 kyr (Figure 25.c 3rd row), the two offsetted red line indicates tensile failure at the termination and the shorter one at the high Z side helps maintain a near ridge axis high angle normal fault. At 430 kyr (Figure 25.d), the presence of vertical tensile failure near the ridge axis at the low Z side is responsible for the recede of the front of the plastic strain at $Z = 1 \sim 3$. While at $Z=5 \sim 10$, the breakaway keeps extending further away from the ridge axis. This curved front results in a curved topography as seen in 640 kyr (Figure 25.e) and is also responsible for the large dextral shear (blue) zone (5th row). At 705 kyr (Figure 25.f), a new near ridge axis

secondary fault begin to evolve and replace the original one at high Z side with a length of \sim 15 kilometers. The secondary fault also connect with the further away from ridge axis original fault at low Z side. The topography at 1000 kyr (Figure 25.h) is a result of the curved and later connected fault. The frontier of the plastic strain at high Z side soon catch up with that at the low Z side due to the presence of a tensile failure zone at the low Z side that has taken up part of the extension.

3.5.4 M28SqrtT1 versus M58SqrtT1

For description of M28SqrtT1 evolution with respect to time, please refer to Paragraph 4 and Figure 30.

For description of M58SqrtT1 evolution with respect to time, please refer to Paragraph 3.4.2 and Figure 22.

3.5.5 M57SqrtT2 versus M58SqrtT2

For description of M58SqrtT2 evolution with respect to time, please refer to Paragraph 3.4.2 and Figure 23.

The major difference between M57SqrtT2 and M58SqrtT2 is that M57SqrtT2 keeps faulting at the same side of the ridge axis while M58SqrtT2 alternates.

M57SqrtT2 For M57SqrtT2, there are totally six small scale cut back happen at 282.5 kyr, 290 kyr, 365 kyr, 452.5 kyr, 482.5 kyr and 540 kyr respectively (the model stops at 540 kyr). As shown in Figure 26, the fault keeps on the left hand side of the ridge axis. At 200 kyr (Figure 26.b), a new near ridge axis high angle normal fault begin to evolve and take the place of the initial one. As the fault evolve, a transient stage of discontinuous abyssal hill is produced at the low Z side as seen at 225 kyr (Figure 26.c). The fault propagate toward high Z side and cut through the plate at \sim 245 kyr (Figure 26.d) when sawtooth shape topography at the low Z side (2nd row) is created by sawtooth shape σ_{xx}

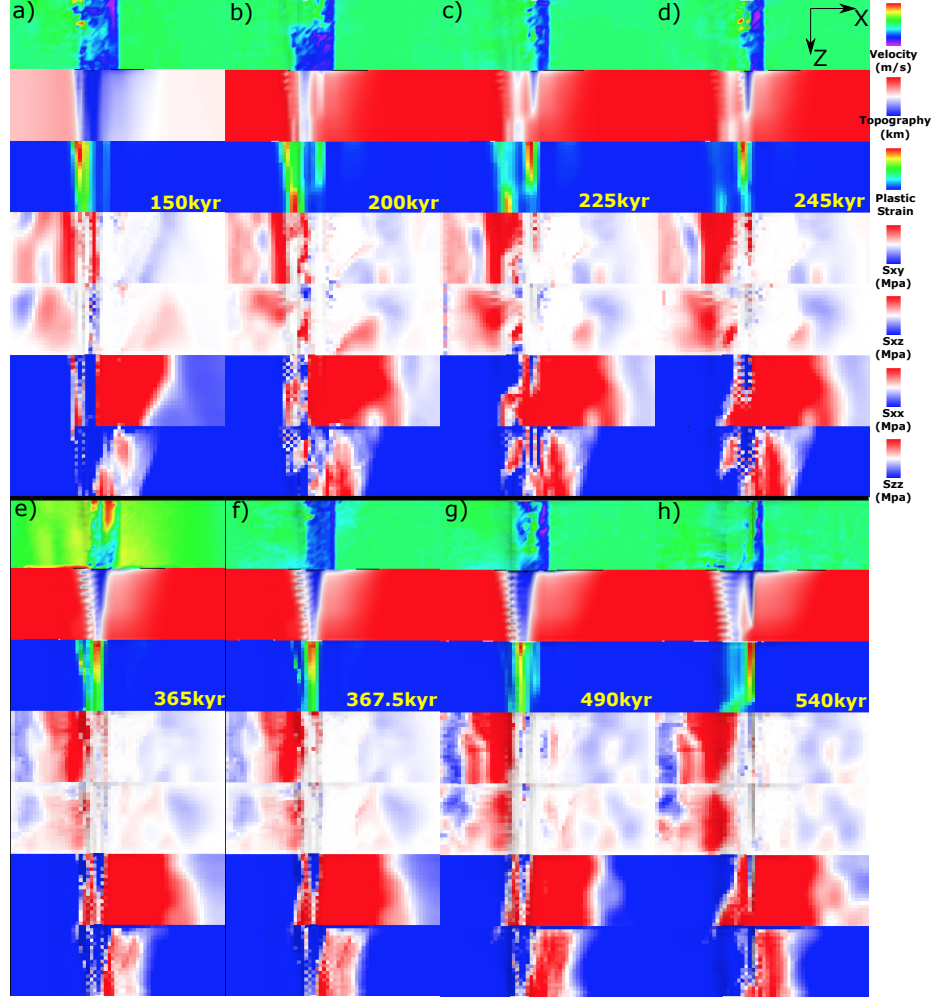


Figure 26: M57SqrtT2 (Table 2) faulting and stress evolution with respect to time.

(6th row) and σ_{zz} (7th row). Between 365 kyr (Figure 26.e) and 367.5 kyr (Figure 26.f), there is a cut back. At 490 kyr (Figure 26.g), there is new near ridge axis antithetic fault on the hanging wall which terminates the old fault and develops into a vertical near ridge axis tensile failure as seen at 540 kyr (Figure 26.h).

3.6 Summary of Results

There are several behaviors that are controlled by the model parameters. Generally, only M58 models with type 2 weakening produce alternating faults on both side of the ridge axis. All the models show corrugations. As for faulting patterns in terms of evolution fre-

quency, usually Square root is more dynamic than Sinusoidal than Linear, M58 is more dynamic than M57 than M28.

Following tables are a summary of the model behaviors with respect to different setup parameters.

Table 3: Model behaviors in short.

A	Alternating Fault	C	Corrugation	SL	Shear Topography Low
NA	Not Alternating	SF	Secondary Fault on one side	CB	Cut Back
DD	Double Dome	AM	Atlantis Massif Shape		

Based on the 11 models with M variation, we observed eight first-order behaviors as shown in Table 3.

Table 4: Linear functional form.

M range Type \ Type	M28	M57	M58
Type one	NA; C; SL; SF _{1500kyr} ; DD	NA; C; SF _{1380kyr} ; CB _{330kyr} ; AM(opposite z)	
Type two			

Table 5: Sinusoidal functional form.

M range Type \ Type	M28	M57	M58
Type one	NA; C; SL; SF _{995kyr}	NA; C; SL; SF _{760kyr;1320kyr} ; CB _{520kyr} ; AM	NA; C; SL; CB _{510kyr} ; SF _{760kyr;1140kyr;1990kyr}
Type two		NA; C; SL; SF _{680kyr} ; CB _{905kyr}	A _{450kyr;600kyr} ; C(only at low M); CB _{990kyr}

Table 6: Square root functional form.

M range Type \	M28	M57	M58
Type one	NA; C; SL; $CB_{205kyr;330kyr;1025kyr}$		NA; $C_{1770kyr}$ (due to shear with dif wave length); SF_{860kyr} (high M); $SF_{1190kyr}$ (low M)(Dog Bone); $SF_{1690kyr}$
Type two		NA; C; $SF_{435kyr;1060kyr};$ $CB_{585kyr}; CB_{735kyr};$ $CB_{910kyr}; CB_{970kyr}$	$A_{550kyr;920kyr}; C;$ CB_{400kyr}

4 Discussion

Generally, all models forms a median valley that deepens and widens toward the lower M side (Figure 8) except the reference model with constant $M = 0.8$ (Figure 11). The topography observed in our models, to the first order, is controlled by the spatial and temporal distributions of faulting and to the second order, results from elastically deformation (e.g. The gradual deepening and widening of the median valley; The bending of the crust at the footwall side of the detachment fault results in a domal shape of the fault interface as a mechanism for producing the dome shape of OCCs).

The pattern of the deformation (faulting and elastic deformation) is controlled by the evolving stress in the crust in terms of its distribution and magnitude. The stress evolution is a result of the interaction processes between tectonics and magmatism. Due to constant seafloor spreading, tensional stress orthogonal to the ridge-axis in the crust keeps accumulating. At the same time, along ridge-axis varying diking partially accommodates the stress from far field extension and perturbs the homogeneity state of stress distribution along the ridge-axis. Accumulated stress will be largely released when the tensile or shear failures establish.

Since the model behavior is very complicated. We will focus on the effects being brought by the along ridge-axis variation in diking. Thus, it is worth considering a thought experiment with two end members: One, the along ridge-axis coupling is rigid, so that even along ridge axis variation in M exist, once a fault determined to develop, it will cut through the whole model domain along the ridge-axis(Z-axis) simultaneously. The other end member is that there is totally no coupling along the ridge-axis. So that each slice of crossection profile across the ridge behave separately without being influenced by its neighbour to a extreme that the model behavior is just a combination of 20 pseudo-2D models piled up along ridge-axis with their own M . (IMPORTANT: this suggests the importance and urgency for making clear conclusion and results description for previous pseudo-2D models results. However, one difficulty here is that the characteristic fault off-

set ΔX_c is different between 2D and 3D models.)

4.1 Discussion on Reference models

4.2 Cut Back

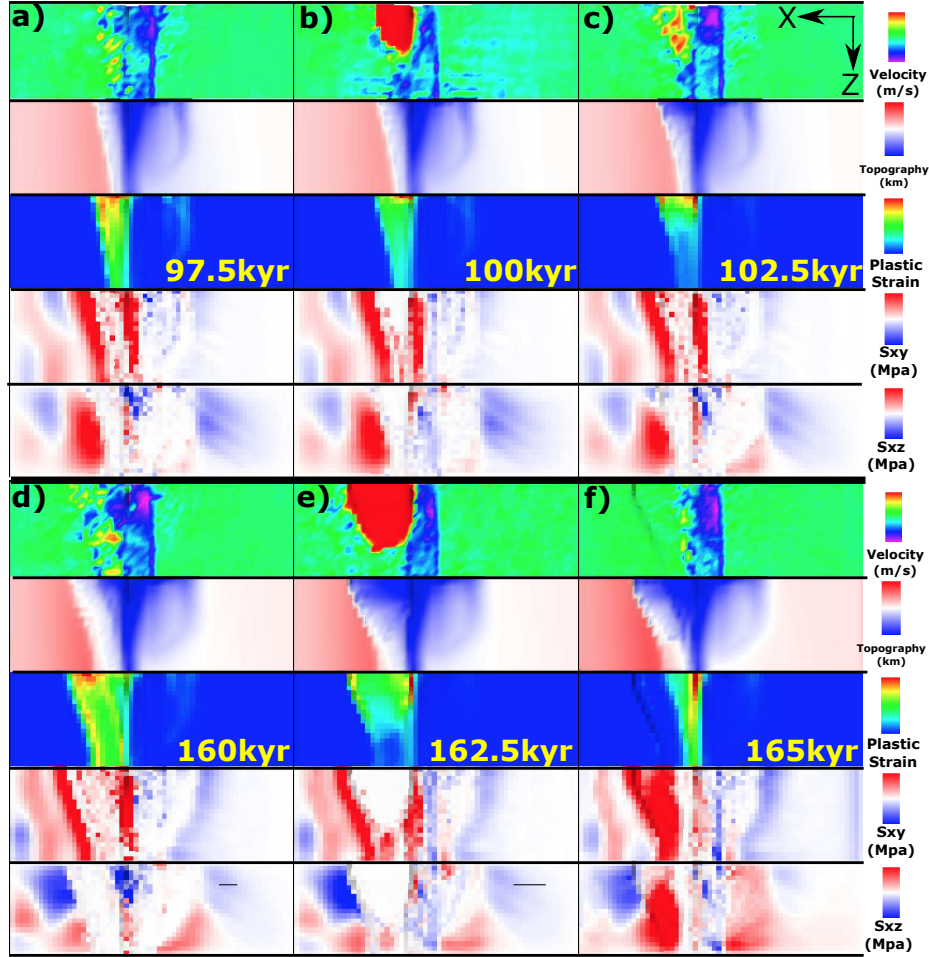


Figure 27: M28SqrtT1 (Table 2). Cut back behaviors in square root functional form model with different time.

The cut back happens mostly in the square root model. Since the linear model and the square root model have more obvious difference in terms of the cut back behavior, here, we only compare linear and square root. There are several factors contribute to the cut back behavior. First, at the higher M side, the amount of diking for the square root model is ubiquitously larger than that of the linear one (Figure 13). This leads to a slower bend-

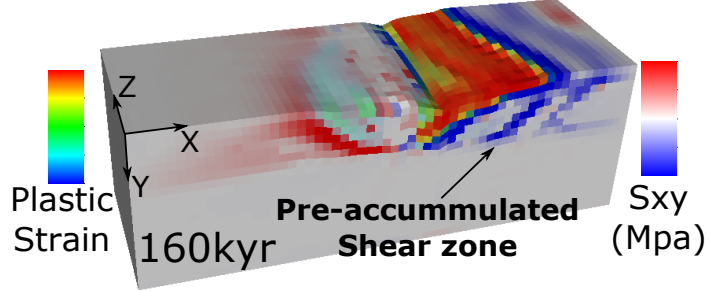


Figure 28: M28SqrtT1 (Table 2). Square root functional form model at 160kyr. Pre-accumulated shear zone increase the shear force and cut the weak detachment front tip

ing detachment at the high M side for the square root model. Second, the total length of the ridge segment with $M > 0.5$ for the square root model is also longer than that of the linear one (Figure 13). This results in that at the low M side, σ_{xz} is focused at low Z adjacent to the ridge-axis (Figure 15.e), however for linear is spread out to Z higher than 10. Third, due to higher value of $\frac{dM}{dZ}$ for square root when $Z < 5$, the along ridge-axis shear σ_{xz} for square root will be accumulating faster, which produces larger strike-slip force to cut the hanging wall at the low M side. Fourth, as observed in the model (Figure 15.c), the parallel to spreading direction offset between breakaways along the ridge-axis is 4km for the square root model compared to 3km for the linear model. This causes the square root model to experience bigger shear stress σ_{xy} both immediately beneath and above the fault interface at the low M side (Figure 15.d). Fifth, as shown in Figure 10, due to bending of the crust at the footwall side, below the blue neutral plane, $\sigma_{xx} > 0$, meaning tensile stress being accumulated as fault develops. The resulting force tends to unbend the bent crust and drag down the connecting surface (the future decoupled hanging wall). All five factors together assist in the decouple of the hanging wall at the low M side as described in detail in the next paragraph.

In the Figure 27, the hanging wall rebounds backwards to the dike in a high velocity (Figure 27.b,e (velocity)) accompanied with a sudden topography drop (Figure 27.b) compared to c); d) compared to e) (in the second row)). This behavior is triggered when

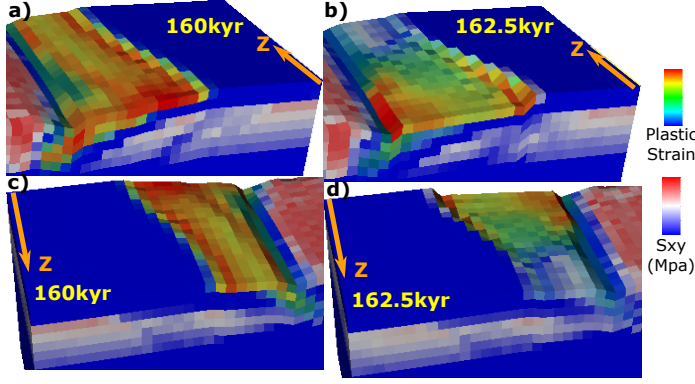


Figure 29: M28SqrtT1 (Table 2). Bending stress drop in the crust close to dike due to cut back behavior.

the front tip of the weak detachment extends further away from the ridge-axis and reaches a pre-accumulated shear zone (Figure 28). The pre-accumulated shear zone adds extra shear force to the weak (Figure 27.d(third row: plastic strain)) as well as shear stresses accumulated (Figure 27.d(fourth and fifth row: σ_{xy} and σ_{xz})) fault interface and together with the five factors mentioned in the previous paragraph result in the cut back behavior. The cut back produces a continuous high angle fault scarp with a relief of $\sim 1\text{ km}$ aligns to the initial breakaway and extends for about 20 kilometer in length (Figure 27.e (second row: topography)). Its distance to the ridge-axis varies along the Z-axis and this result can be used to indicate the magma supply variation in the nature. ^{XT:}To be discussed in observation comparison section. as a reminder

During the cut back process, the tensional bending stress are released at the low M side ($0 < Z < 7$) in the left tip of the bended crust (Figure 29.a compared to b), however, in the higher M side, the tensional bending stress keeps accumulating due to the far field extension (Figure 29.c compared to d). This behavior assists in the decouple between low M and high M side hanging walls.

Once the cut back happens at 162.5kyr, the σ_{xy} , σ_{xz} and σ_{xx} are released (Figure 27.e (fourth and fifth row: σ_{xy} and σ_{xz})). The plastic strain near the ridge-axis at low M side reaches a maximum of ~ 0.9 (Figure 27.e (third row: plastic strain)) compared to ~ 0.3 before and after. This is due to the sudden backward motion squeezes the end element of

the hanging wall near the ridge-axis and later be released by the continuous extension.

After the cut back, the termination of the detachment recedes backwards for about 7 kilometer towards the ridge-axis (Figure 27.f (third row: plastic strain)) (termination fronts are always consistent with tension stresses in σ_{xx} and σ_{zz} as well as with plastic strain front(due to healing, high plastic strain region corresponds only to region with continuously deformation) (Figure 15 and Figure 16)). This behavior helps maintain a high angle normal fault. Different from the linear and sinusoidal models that the detachments at the low M side will rotate to a very low angle, square root model doesn't. In addition, σ_{xy} and σ_{xz} soon fill in the area between cut back created fault scarp and the new termination (Figure 27.f (fourth and fifth row: σ_{xy} and σ_{xz}) because σ_{xy} always accumulates immediately beneath the normal fault interface and the red σ_{xz} left to the new termination is due to the along ridge-axis variatioin in the rate of fault slip (low M side larger).

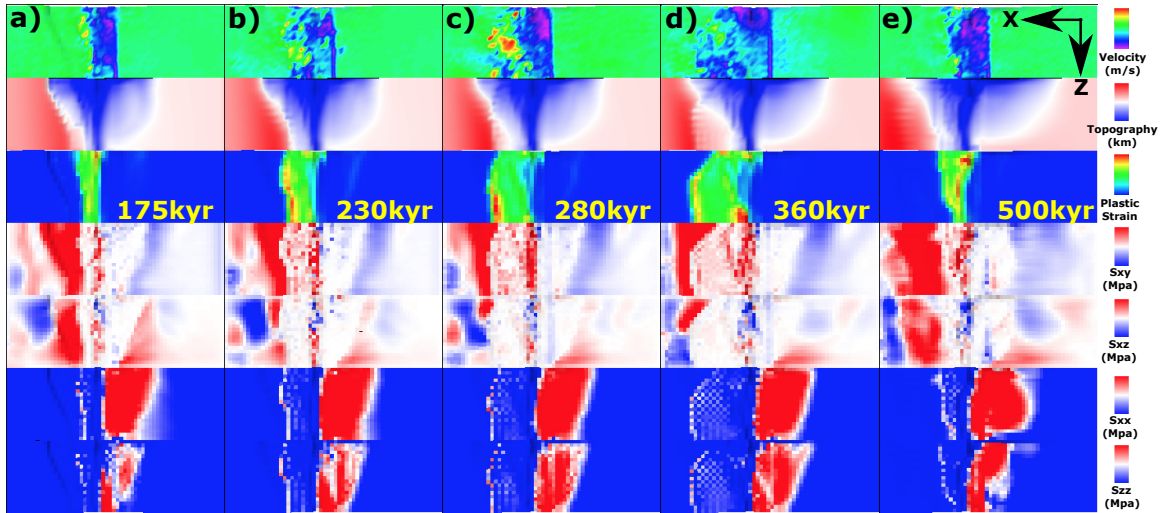


Figure 30: M28SqrtT1 (Table 2). New fault front chase after initial abandoned breakaway.

There is one phenomenon very interesting and counter-intuitive that worth describing here. After the cut back, and termination retreat, the evolution of the detachment fronts is opposite to initiall or to the general behavior in the linear and sinusoidal models. The termination front at the high M side extends faster and further after the cut back (Figure 30). This is partly related to the unbending decouple phenomenon we described ealier that the

tensional stress are released at the low M side but continues to accumulate in the high M side during the cut back unbending in the low M side. Since the tensional stress is released in the low M side, it needs time to accumulate to where it was and then start from there to drag the new near ridge-axis fault away from the ridge-axis while at the high M side the increasing tensional stress will directly lead to a fast extending fault front. Thus create the behavior. *^{XT}: One question is, how to explain that the fault front is moving much faster than the initial abandoned breakaway? New fault front soon reach the old breakaway.*

This phenomenon is largely responsible for the corrugations observed. It creates a “X” shape “scan” that first “scan” the topography with faster low M side (Figure 27.d and e) and then with faster high M side (Figure 30.c and d). This results in curved terminations with hundreds to several kilometers wavelengths that directly create parallel to spreading direction corrugations.

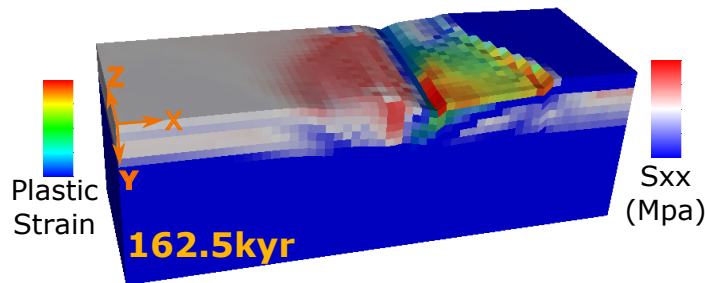


Figure 31: M28SqrtT1 (Table 2). Higher σ_{xx} in the median valley of conjugate plate at low M side.

In addition, the higher σ_{xx} in the median valley of conjugate plate at low M side (Figure 31) is due to the brittle crust is thinnest at the median valley, thus when same amount of force propagates from far field extension to the center median valley, the stress will increases.

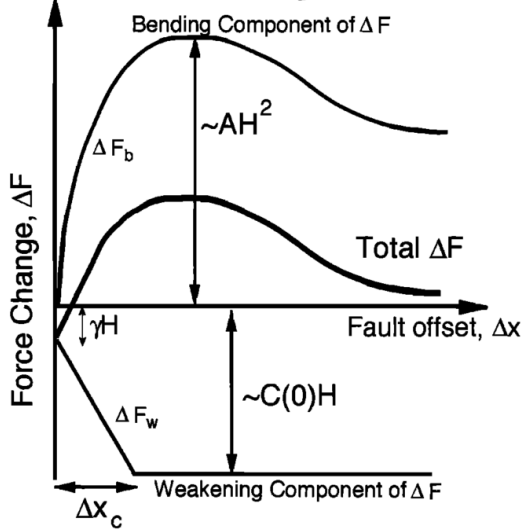


Figure 32: Trade-off between change in bending force ΔF_b and weakening in the fault interface ΔF_w . H is the thickness of the brittle crust and γ is the size of initial weak perturbation and A defines the maximum bending force change. (For more details, please refer to [Lavier et al., 2000])

4.3 Fault Alteration

4.3.1 Trade-off between bending and weakening

Before we move on to each of the pairs, the framework studied by [Lavier et al., 2000] needs to be mentioned here for better understanding the model behaviors observed in our model results. There is a trade-off between change in bending force ΔF_b as a function of fault offset ΔX and force change ΔF_w as a function of ΔX due to strain weakening. As described in [Lavier et al., 2000], higher characteristic fault offset (ΔX_c) or slower strain weakening results in multiple faults rather than only one fault lasting. Whether conjugate fault and even multiple faults can be produced depends on the local stress condition. The strength weakening of the existed fault combines with how much bending force resists the fault to keep offsetting play a major role in determining the stress state at the other areas. As the sea-floor keeps spreading and ΔX increasing, the change in bending force ΔF_b increases and the strength at the fault interface decreases due to weakening ΔF_w (Figure 32). If the net force change $\Delta F = \Delta F_b + \Delta F_w$ is positive, it means that it is

getting harder and harder to maintain the existing fault and stress will begin to accumulate at the other areas which eventually break another fault. ΔF_b initially increases fast with respect to ΔX and then when the breakaway bends over, it reaches its peak value and begins to decrease a little and maintains at a constant value. If the strain weakening is fast enough that the net effect force ΔF is always negative, then most of the stress will be released by the existing fault and thus no conjugate or multiple faults will be created.

Our model results verify this analysis that only Type two weakening (slower weakening with higher ΔX_c) can produce an alternating normal fault on the conjugate plate.

Based on the previous experience in pseudo-2D models and [Lavier et al., 2000], when $M > 0.5$, the frequency of normal faulting alternation is higher for higher characteristic fault offset (ΔX_c) of Type two weakening compared to Type one weakening. However, for the reference model two, M88ConT2 (Table 2), interesting enough, when comparing pseudo-2D and 3D models with Type two weakening under case of $M = 0.8$, even though the 3D Model has a larger ΔX_c of 1km than that of pseudo-2D model of 0.5km, the 3D model M88ConT2 has a lower frequency of faulting alternation. Since M is constant 0.8 along the ridge-axis, the effect of along ridge coupling that resists alternation need not be considered. One possibility is that the resisting bending force increase in a higher rate than linear with respect to increasing the length of the ridge segment (Z_{max} km).

4.3.2 Alternating on conjugate plate

The fault alternation behavior observed in pseudo-2D models in cases $M > 0.5$ is much more complicated in 3D models. The results show that only Type two weakening with M58 will result in an alternating faulting pattern. XT : integrate the area of $M > 0.5$ with respect to Z to see if there is any quantitative analysis available.

4.3.3 Secondary near-axis normal fault

The secondary near axis high angle normal fault is another common observation of the models. As shown in Figure 8, at the ridge axis with $M > 0.5$ (i.e. $Z > 10$), the existing normal fault will be pushed away from the ridge-axis due to excessive diking, as its mechanism has been mentioned in the introduction chapter, another new near axis normal fault is created at around 650kyr. As it evolves, the initial detachment fault becomes inactive (the transparent view of plastic strain shown in the right corner inset of time 880kyr). This secondary fault creates another dome and its composition is more likely to be volcanic rather than ultramafic, however, as it evolves, if it can last long, lower crust and upper mantle material can be exhumed to the surface. The composition of the domes observed at Kane magamullions is similar to this mechanism that ultramafic Babel dome is on the West and crustal inside-corner high on the East.

4.3.4 Effect of along ridge-axis coupling

The along ridge-axis coupling allowed the normal fault at the high M side ($M > 0.5$) to last for a long time and become a detachment that can produce an OCC. This behavior is different from previous 2D studies that only $M=0.3 \sim 0.5$ can make OCCs and it also provides an alternative explanation for reconciling the gap between 2D model and observation described in [Olive et al., 2010]. Instead of magma injecting below brittle ductile transition, even injecting in the crust, due to along ridge coupling, model can still create OCC for high magma supply. Find the observation evidence for high M OCC from refs of Olive2010. As mentioned in the abstract of Olive2010, ref4-11 show a spectrum of magma supply.

4.4 Corrugations

There are two contributing factors, for one, trans-extenstional stresses are created due to offset of the breakaway as well as the variation in fault displacements along the ridge axis; for the other, the variation of the positions of the terminations of the detachment faults along the ridge-axis creates anastomosing faults that is mentioned in [Smith et al., 2014]. This anastomosing faulting behavior is largely responsible for corrugations in our models.

The stress at the tips of the breakaways is generally tensional in both parallel and orthogonal directions to the ridge-axis. (Figure 15.f,g)

4.4.1 Wavelength of corrugations

4.5 Influence of healing

4.6 Comparing model results with nature observation

4.6.1 Cut back at 13°N Mid-Atlantic Ridge (M28SqrtT1)

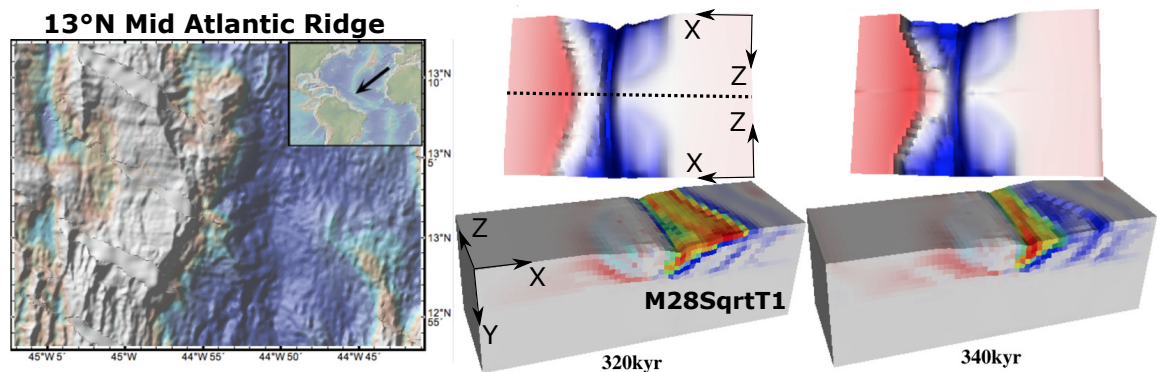


Figure 33: Comparing nature observation at 13°N Mid-Atlantic Ridge to the Cut back behavior of model M28SqrtT1. The model topography is a mirror symetric flip according to the dash line, it reveals the case of M varies in a square root functional form from 0.2 to 0.8 to 0.2. For discussion on cut back formation mechanism, please refer to Section 4.2. The bathymetry is from GeoMapApp [Ryan et al., 2009].

The cut back behavior in M28SqrtT1 model creates a fault scarp of $\sim 1\text{km}$ in relief,

40km in length along the Z axis. Note that the fault scarp corresponds to initial formed breakaway. The topography at 13°N Mid-Atlantic Ridge also has a fault scarp with very similar geometry with ~1km in relief. Due to the variation in diking along the ridge-axis, a sandglass shape of median valley is also produced in the model where the narrowest center corresponds to the region with high magma supply ($M=0.8$). This sandglass shape is also frequently observed in the nature along the Mid-Atlantic Ridges.

4.6.2 Double dome at 23°N Mid-Atlantic Ridge (Kane Megamullions) (Several models)

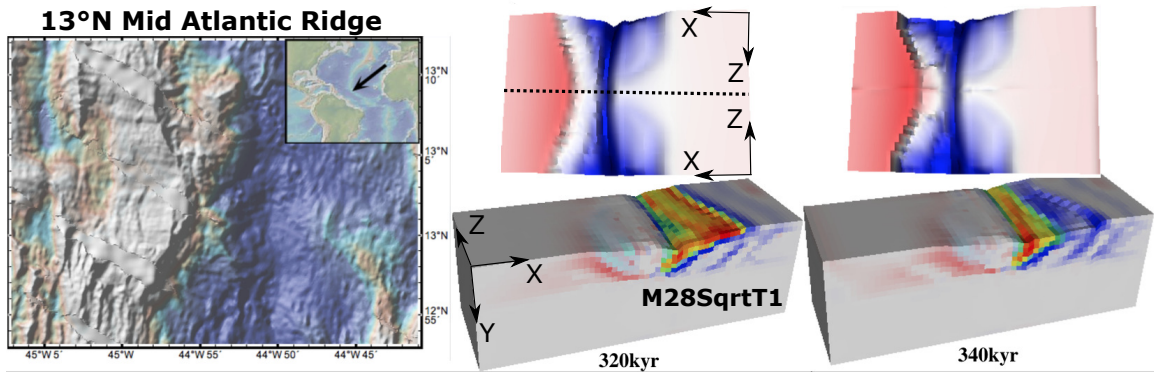


Figure 34: Comparing nature observation at 13°N Mid-Atlantic Ridge to the Cut back behavior of model M28SqrtT1. The model topography is a mirror symmetric flip according to the dash line, it reveals the case of M varies in a square root functional form from 0.2 to 0.8 to 0.2. For discussion on cut back formation mechanism, please refer to Section 4.2.

4.6.3 Atlantis Massif Shape at 30°N Mid-Atlantic Ridge ()

4.6.4 Shear low

4.6.5 Corrugations

4.7 Model Limitation

4.7.1 Fixed thermal structure effects and justification

Thermal conduction rate for $\kappa = 6\text{mm}^2/\text{s}$ material is $1.8\text{e}5 \text{ km/Myr}$, four magnitude faster compared to spreading rate of 2.5km/Myr .

4.8 Recommendation for Future Research

Bibliography

- G. Baines, M. J. Cheadle, B. E. John, and J. J. Schwartz. The rate of oceanic detachment faulting at atlantis bank, sw indian ridge. *Earth and Planetary Science Letters*, 273(1-2):105–114, Aug. 2008. ISSN 0012821X. doi: 10.1016/j.epsl.2008.06.013.
- R. Buck, L. Lavier, and A. Poliakov. Modes of faulting at mid-ocean ridges. *Nature*, 434(7034):719–23, 2005. ISSN 1476-4687. doi: 10.1038/nature03358.
- S. M. Carbotte, D. K. Smith, M. Cannat, and E. M. Klein. Tectonic and magmatic segmentation of the global ocean ridge system : a synthesis of observations. *Geological Society of London*, 2015.
- Y. J. Chen and J. Lin. Mechanisms for the formation of ridge-axis topography at slow-spreading ridges: A lithospheric-plate flexural model. *Geophysical Journal International*, 136:8–18, 1999. ISSN 0956540X. doi: 10.1046/j.1365-246X.1999.00716.x.
- E. Choi, L. Lavier, and M. Gurnis. Thermomechanics of mid-ocean ridge segmentation. *Physics of the Earth and Planetary Interiors*, 171(1-4):374–386, Dec. 2008. ISSN 00319201. doi: 10.1016/j.pepi.2008.08.010.
- C. M. R. Fowler. *The solid earth: an introduction to global geophysics*. Cambridge University Press, 2004.
- S. Kirby and A. K. Kronenberg. Rheology of the lithosphere: Selected topics. *Reviews of Geophysics*, 25(6):1219–1244, 1987.
- L. L. Lavier, W. R. Buck, and A. N. B. Poliakov. Factors controlling normal fault offset in an ideal brittle layer. *Journal of Geophysical Research*, 105(B10):23431, 2000. doi: 10.1029/2000JB900108.
- J. Lin, G. M. Purdy, H. Schouten, J.-C. Sempere, and C. Zervas. Evidence from gravity

data for focused magmatic accretion along the Mid-Atlantic Ridge. *Nature*, 344:627–632, 1990. ISSN 0028-0836. doi: 10.1038/344627a0.

J.-A. Olive, M. D. Behn, and B. E. Tucholke. The structure of oceanic core complexes controlled by the depth distribution of magma emplacement. *Nature Geoscience*, 3(7):491–495, June 2010. ISSN 1752-0894. doi: 10.1038/ngeo888.

W. B. F. Ryan, S. M. Carbotte, J. O. Coplan, S. O’Hara, A. Melkonian, R. Arko, R. A. Weissel, V. Ferrini, A. Goodwillie, F. Nitsche, J. Bonczkowski, and R. Zemsky. Global multi-resolution topography synthesis. *Geochemistry, Geophysics, Geosystems*, 10, 2009. ISSN 15252027. doi: 10.1029/2008GC002332.

D. K. Smith, H. Schouten, H. J. B. Dick, J. R. Cann, V. Salters, H. R. Marschall, F. Ji, D. Yoerger, A. Sanfilippo, R. Parnell-turner, C. Palmiotto, A. Zhelezov, H. Bai, W. Junkin, B. Urann, S. Dick, M. Sulanowska, P. Lemmond, and S. Curry. Development and evolution of detachment faulting along 50 km of the mid-atlantic ridge near 16.5°n. *Geochemistry Geophysics Geosystems*, pages 4692–4711, 2014. doi: 10.1002/2014GC005563. Received.

M. Tolstoy, A. J. Harding, and J. A. Orcutt. Crustal Thickness on the Mid-Atlantic Ridge: Bull’s-Eye Gravity Anomalies and Focused Accretion. *Science*, 262(October):726–729, 1993. ISSN 0036-8075. doi: 10.1126/science.262.5134.726.

B. E. Tucholke, M. D. Behn, W. R. Buck, and J. Lin. Role of melt supply in oceanic detachment faulting and formation of megamullions. *Geology*, 36(6):455, 2008. ISSN 0091-7613. doi: 10.1130/G24639A.1.

D. L. Turcotte and G. Schubert. *Geodynamics*. Cambridge, 2002.